Available online at www.sciencedirect.com
SCIENCE DIRECT
Journal of Catalysis 242 (2006) 92–102
JOURNAL OF CATALYSIS
www.elsevier.com/locate/jcat

Syngas by catalytic partial oxidation of methane on rhodium: Mechanistic conclusions from spatially resolved measurements and numerical simulations

R. Horn *, K.A. Williams, N.J. Degenstein, L.D. Schmidt

Department of Chemical Engineering and Materials Science, University of Minnesota, 421 Washington Avenue SE, Minneapolis, MN 55455, USA

Received 9 March 2006; revised 6 May 2006; accepted 10 May 2006

Available online 3 July 2006

Abstract

The mechanism for the catalytic partial oxidation of CH_4 on Rh-coated α-Al_2O_3 foam monoliths was investigated by measuring species and temperature profiles along the catalyst axis and comparing them with numerical simulations. A thin quartz capillary connected to a quadrupole mass spectrometer was moved through the catalyst with a spatial resolution of ~0.3 mm. Profiles were measured under autothermal operation for C/O ratios of 0.7, 1.0 and 1.3. The influence of the flow rate (5 vs. 10 l min^{-1}) was studied for syngas stoichiometry (C/O = 1). Numerical simulations were performed with a 38 step surface mechanism using both a porous 2D-model with mass and heat transfer and a simple plug-flow model. The experimental profiles reveal complete O_2 conversion within 2 mm of the catalyst entrance for all C/O ratios and flows. H_2 and CO are formed partly in the oxidation zone and partly after O_2 is fully converted by steam reforming. CO_2 is formed in small amounts in the oxidation zone and remains constant thereafter, except for C/O = 0.7, where some water gas shift is observed. CO_2 reforming does not occur under the experimental conditions. Based on the experimental findings, a two-zone picture of the reaction mechanism is proposed. The 2D numerical simulations and the measured profiles agree qualitatively for all experimental conditions. Quantitative agreement is best for syngas stoichiometry (C/O = 1.0) at 5 and 10 l min^{-1} flow rate. Some quantitative differences are observed for C/O = 0.7 and 1.3. The plug flow model is for all conditions inferior to the 2D model. The importance of spatial profiles for mechanism and reactor model validation is highlighted.

Keywords: Syngas; Catalytic partial oxidation; Methane; Mechanism; Rhodium; Mass spectrometry; Spatial profiles; Numerical simulation

1. Introduction

The conversion of methane into hydrogen, liquid fuels, or chemicals is of growing economic importance. Natural gas, which consists mainly of methane, is available in similar amounts on earth as oil, but it is far less exploited. According to recent assessments, oil production will peak before the year 2040 [1]. Strong efforts in science and technology are underway to convert natural gas into liquids to open up a large petroleum resource that can compensate potential oil shortfalls [2].

The first step in the transformation of methane to liquids is the production of syngas. The catalytic partial oxidation (CPO) of methane (Eq. (1)) on Rh-coated foam monoliths is an efficient way to achieve this transformation [3]. In contrast to the highly endothermic steam reforming (Eq. (2)), the CPO reaction (1) is slightly exothermic.

$$CH_4 + (1/2)O_2 \rightarrow CO + 2H_2, \quad \Delta H_r^\circ = -36\ \text{kJ mol}^{-1}, \quad (1)$$

$$CH_4 + H_2O \rightarrow CO + 3H_2, \quad \Delta H_r^\circ = +206\ \text{kJ mol}^{-1}. \quad (2)$$

Steam reforming on Ni requires contact times in the range of 1 s to achieve sufficient CH_4 conversion. For the CPO reaction on Rh, CH_4 conversion close to 100% and >90% selectivities to H_2 and CO can be achieved in a few ms [4]. CPO reactors can be operated autothermally and with a much higher gas hourly space velocity than a steam reformer, making them attractive for remote gas field applications. For process integration, methane CPO supplies a H_2/CO ratio of 2 that is more favorable for downstream chemistry (methanol, Fischer–Tropsch synthesis) than the higher ratio obtained by steam reforming.

* Corresponding author.
E-mail address: horn@cems.umn.edu (R. Horn).

0021-9517/$ – see front matter
doi:10.1016/j.jcat.2006.05.008

1.1. Experimental studies on the CPO mechanism

There is an ongoing debate about the mechanism of the methane CPO. The present literature review focuses on results on Rh, but similar arguments may hold for other catalysts. A direct mechanism (pyrolysis–oxidation) and an indirect (combustion–reforming) mechanism are discussed in the literature [5]. The pyrolysis–oxidation mechanism assumes that H_2 and CO are primary reaction products formed in the oxidation zone at the catalyst entrance. After methane pyrolysis ($CH_4 \rightarrow C_s + 4H_s$), surface carbon reacts with surface oxygen to CO ($C_s + O_s \rightarrow CO$) and surface hydrogen atoms combine to H_2 ($H_s + H_s \rightarrow H_2$). In contrast, the combustion-reforming mechanism postulates a two-zone model with a CH_4 combustion zone at the catalyst entrance ($CH_4 + 2O_2 \rightarrow CO_2 + 2H_2O$), and H_2 and CO production in a reforming zone downstream ($CH_4 + H_2O \rightarrow CO + 3H_2$, $CH_4 + CO_2 \rightarrow 2CO + 2H_2$, respectively).

Because the mechanisms postulate different reaction zones, spatially resolved measurements would help verify the assumptions; however, only one paper reporting intracatalyst species and temperature profiles (at high pressures, 0.2–0.8 MPa) has been published so far. Lyubovsky et al. [6] used a stack of Microlith® screens and measured species and temperature behind each screen. They argued for mainly direct formation of CO and indirect formation of H_2 by steam reforming. This conclusion was drawn by extrapolating CO and H_2 selectivities to zero CH_4 conversion. But because the spatial resolution was only 2 mm, and the CH_4 and O_2 conversion at the first point were already 40% and >80%, respectively, extrapolation over such a large range could be imprecise. With the capillary technique used in the present paper, 0.3 mm resolution has been achieved.

Nonspatially resolved investigations into the mechanism are numerous in the literature. Among these are some supporting the direct mechanism [7–12], some supporting the indirect mechanism [13–15], and others supporting a mixed mechanism [6,16]. In some cases, the mechanistic conclusions contradict each other. However, the literature results indicate a dependence of the mechanism on (i) temperature [10,17–19], (ii) pressure [13], (iii) Rh oxidation state [8,11–14,16,18,19], (iv) catalyst loading [11,17], and (v) nature of the support [8,14,15,18,20]. Therefore, contradictions may arise because the mechanistic conclusions cannot be extrapolated beyond the conditions of the particular experiment.

Without discussing individual results, an overall picture of the reaction can be extracted from the studies cited above. It seems that reduced Rh sites (Rh metal) are active for syngas production with CH_4 dissociation as the rate-limiting step. Oxidized Rh sites (Rh_xO_y) lead to the formation of total oxidation products (H_2O, CO_2). The oxidation state of the Rh surface depends on temperature and gas atmosphere. Many studies report CO_2 and H_2O formation after the reaction was started on an oxidized Rh catalyst, but the selectivities turn to syngas formation after a short operational time, because reduced Rh sites are formed. At high temperatures, the overall gas atmosphere is sufficiently reducing to restore metallic Rh sites quickly even if gas-phase oxygen is present. Chemisorbed oxygen can lead to total oxidation if the surface temperature is low (e.g., 500 °C). In this case H_2 and CO are not desorbing quickly enough and become oxidized. The higher the temperature, the higher the selectivity to H_2 and CO. Most published studies agree that CO_2 reforming is unimportant in the reaction network. It seems that the support is important, especially at low Rh loadings. Some oxides can serve as an oxygen source for the Rh surface (inverse spillover of OH or H_2O), even though the intrinsic catalytic activity of the support is low.

1.2. Numerical studies on the CPO mechanism

As with the experimental studies, the numerical studies published differ in their conclusions about the reaction mechanism. The original papers from Hickman and Schmidt assumed the direct mechanism, because a high-temperature surface model (19 reactions) was developed that described the experimental conversion and selectivity data reasonably well [4,21]. In this model, CH_4 dissociation on metallic Rh sites was lumped into a single step, and H_2 and CO were formed according to the pyrolysis–oxidation mechanism. Except for CO_2 adsorption, all adsorption–desorption steps in this original surface mechanism were reversible. Therefore, steam reforming was not excluded by definition, but CO_2 reforming was excluded (low sticking coefficient of CO_2 on Rh). A 2D simulation using that mechanism showed no contribution of steam reforming [22]; it was too slow under the given conditions. A plug-flow study using the 19 step surface model and a gas-phase mechanism with 227 reversible reactions (GRI-Mech 2.11) showed that gas-phase reactions were insignificant for atmospheric pressure but become important at elevated pressures (>5 bar) [22–24]. Experimental results corroborate this [13]. Gas-phase reactions are usually not considered in atmospheric pressure simulations.

The mechanism was further improved by including steam reforming and water–gas shift (38 reactions) [25]. CO_2 readsorption was also included. These refinements are in better agreement with experiments showing that steam reforming on Rh is possible in ms contact times [25–27]. The 38 step surface mechanism has been validated against integral steady-state [28,29] and transient experimental data [30,31]. Coverage-dependent desorption energies for CO and O_2 were included [30], because they are important for light-off agreement. The 38 surface reaction step mechanism without coverage dependencies [28] was used in the present publication to compare numerical simulations with experimental spatially resolved profile measurements.

Another, much more extensive C1 mechanism on Rh (104 reactions) was recently reported by Mhadeshwar and Vlachos [32]. All activation energies in this mechanism are coverage-dependent, temperature-dependent, or both. Besides methane CPO, this mechanism also considers methane reformation by water and CO_2 and decomposition of oxygenates on Rh. For methane CPO, this mechanism predicts distinct oxidation (CO_2 and H_2O are products) and reforming (CO and H_2 are products) zones. According to Mhadeshwar and Vlachos, there is

no H_2 formation in the oxidation zone for experiments closely matching the present work.

Our experiments and simulations were motivated by the following conclusions from the literature:

(i) Mass transport, heat transport, and chemistry are strongly coupled in this reaction. Mechanistic conclusions from low-pressure studies (e.g., temporal analysis of products) and from studies with highly diluted reactants or catalysts have to be verified for higher pressures and higher reactant concentrations ⇒ Experimental data must be measured as close to technically relevant conditions as possible.

(ii) Integral conversion and selectivity data can be described equally well by different mechanisms ⇒ Numerical simulations must be compared with experiments with higher information content-here, spatially resolved data.

2. Materials and methods

2.1. Experimental

2.1.1. Reactor configuration and capillary sampling

The reactor setup and capillary sampling system are shown schematically in Fig. 1. The reaction was carried out in a quartz tube (i.d. = 19 mm, length = 40 cm). High-purity reactants CH_4, O_2; and the internal standard Ar were fed through calibrated mass flow controllers through a side port at the bottom of the tube and left the reactor from the top for incineration. An injection needle inserted through a septum at an end port at the bottom of the tube enabled guided movement of the capillary without noticeable gas losses. The exact inlet gas flow rate passing the catalyst was measured for each experiment using a film flow meter at the reactor outlet. All total flow rates specified in this work refer to 20 °C.

α-Al_2O_3 foams (length = 10 mm, diameter = 16.5 mm) with 80 pores per linear inch (ppi, average pore size ∼0.25 mm) with a Rh loading of ∼6 wt% were used as catalysts. The Rh loading was applied to the catalyst foams using the incipient wetness method. An exact calculated amount of $Rh(NO_3)_3$ solution was dropped evenly and in multiple steps to the weighed foams. After each step, the foams were dried at room temperature in vacuum and finally calcined for 6 h at 600 °C in a furnace. A washcoat was not applied. To avoid axial radiative heat losses in the reaction tube, two uncoated α-Al_2O_3 foams were used as heat shields. To avoid bypassing of gas, the catalyst and the heat shields were tightly wrapped in alumo-silicate paper (not shown in Fig. 1).

The reaction profiles were measured by sliding a 20 cm long fine quartz capillary (i.d. = 0.53 mm, o.d. = 0.65 mm, Chrom Tech) through a channel, diamond drilled through the centerline

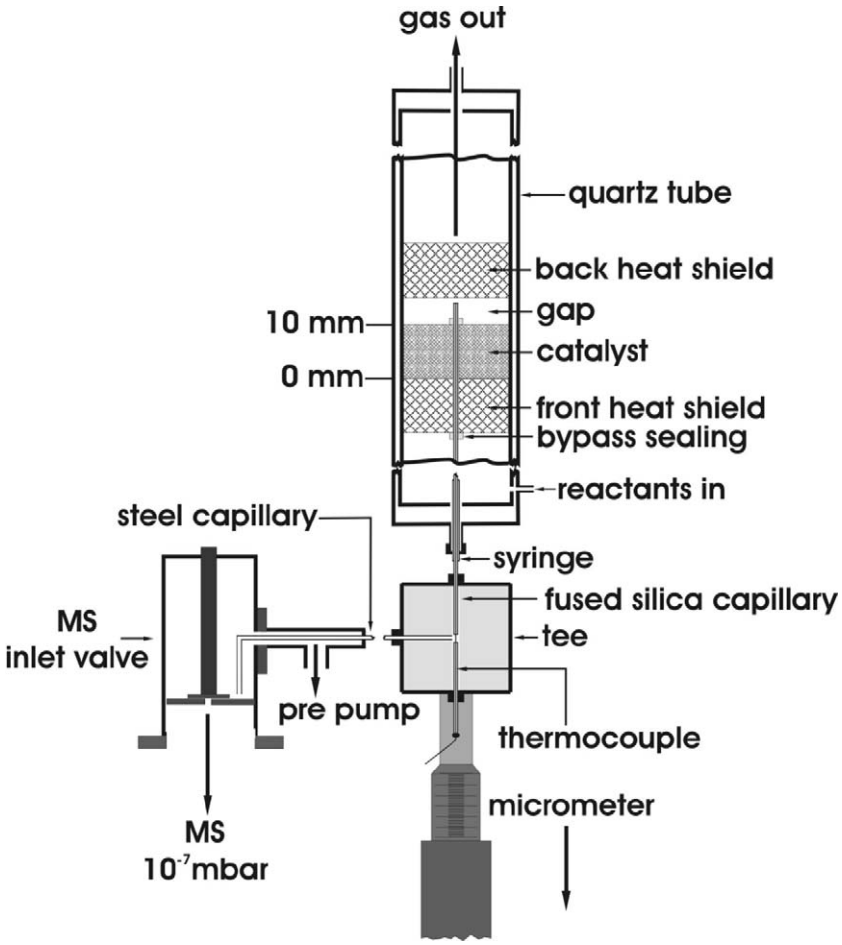

Fig. 1. Reactor setup and capillary sampling system.

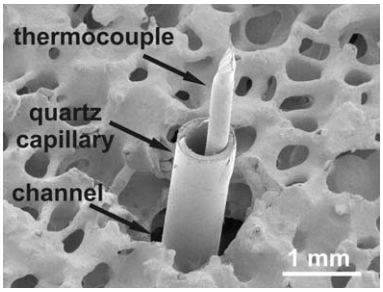

Fig. 2. SEM micrograph showing sampling capillary and thermocouple in a 80 ppi foam.

of the catalyst. The SEM image shown in Fig. 2 was made for illustrative purposes to give an impression of the diameter of the capillary compared with the pores. The channel shown is larger than that actually used (Fig. 2: $d_{\text{channel}} \approx 1$ mm, used: $d_{\text{channel}} \approx 0.8$ mm). Even though the capillary fit tightly into the channel, gas bypassing was further prevented by sealing the capillary entrance and exit with small pieces of alumo-silicate paper (cf. Fig. 1).

The lower end of the capillary was connected to a ported micro-volume tee ($1/16''$, $0.029''$ bore, Valco). The opposite port was used to feed a type K thermocouple into the capillary. The tip of the thermocouple was aligned flush with the open end of the capillary to measure species composition and temperature simultaneously at each point in the catalyst (not aligned in Fig. 2 for illustration). The side port of the tee was connected to a stainless steel capillary ($l \approx 200$ cm, i.d. $= 0.010''$, o.d. $= 1/16''$), which was inserted into the inlet valve of the mass spectrometer vacuum chamber. At the end of the stainless steel capillary, a rotary vane pump generated a vacuum of about 500 mTorr, forcing a permanent flow from the end of the quartz capillary positioned in the catalyst to the sapphire seat of the MS inlet valve. The volumetric flow rate at atmospheric pressure through the capillary was measured as <10 ml min^{-1}, leading to a negligible disturbance of the flow field in the catalyst. Numerical simulations showed that the axial velocity in the catalyst varied from $\sim$0.75 to 2 m s^{-1} depending on the location. The tee was mounted on a micrometer so that the capillary could be moved up and down with sub-mm resolution. All profiles were measured by sliding the capillary tip down (i.e., against the flow direction) from a position 3 mm downstream the end of the catalyst through the catalyst up to about 5 mm into the front heat shield. Using this technique, the open channel is left downstream of the capillary tip and does not influence the sample composition at the tip position. A spatial resolution of $0.0125'' = 0.3175$ mm was used, corresponding to 57 points/profile. All position values presented in Section 3.1 might be off by a positioning error of ± 0.25 mm.

2.1.2. Mass spectrometric analysis

The mass spectrometer used for this study was a quadrupole instrument (UTI model 100C) with an electron impact ionizer (ionization energy 70 eV) and an electron multiplier as a detector. The mass spectrometer was calibrated for H_2 $m/z = 2$ amu, CH_4 $m/z = 15$ amu, CO $m/z = 28$ amu, O_2 $m/z = 32$ amu, and CO_2 $m/z = 44$ amu using Ar $m/z = 40$ amu as an internal standard. In all measurements, the Ar/O_2 ratio was 79/21 close to that in experiments with air used as an oxidant. About 150 full mass spectra were recorded for every point in a profile measurement. After calculation of the mean and substraction of the baseline, the peak areas for the species of interest were calculated by numerical integration using the trapezoidal rule. The Ar-normalized signals were then converted into molar flow rates using the sensitivity factors from the calibration. Besides the contribution from CO_2 to the CO signal at 28 amu, cross-sensitivities were negligible.

Even though all transfer lines and the MS vacuum chamber were heated, H_2O adsorption could not be fully avoided, and the experimentally water signal was not used as the profile. Water was calculated by closing the oxygen balance with it. The C atom balance typically closed better than $\pm 5\%$. The H atom balance was similarly good for most of the points; only in the region of steep gradients (-2 to $+2$ mm) did the H atom balance reach $+20\%$ at some points.

2.2. Numerical simulations

2.2.1. Plug-flow reactor model

In one ideal embodiment of the model reacting system, a single cylindrical hypothetical pore of a 10 mm long 80 ppi foam monolith was simulated using a plug-flow reactor (PFR) model and a nominal diameter of 0.25 mm (assumed ratio of area/volume $= 160$ cm^{-1}) [33], effectively neglecting the tortuous pore network found in ceramic foams. The differential algebraic equations resulting from the plug-flow treatment were solved using the Chemkin PLUG [34,35] or Detchem Plug code [36]. Intrinsic catalyst activity was included through the assumed site density for the Rh surface, which was 2.72×10^{-9} mol cm^{-2} for the 38 step mechanism (for mechanism details see Section 1.2).

2.2.2. 2D porous model

A 2D axisymmetric porous model was used to simulate the reactor conditions at steady state and intra-construct species profiles using computational fluid dynamics (CFD). This model incorporated the entire reactor geometry and dimensions. Because of radial symmetry, only half of one axial cross-section of the reactor tube was considered.

The grid is comprised of the fluid zone (i.d. $= 19$ mm) and the reactor wall (quartz tube, o.d. $= 22$ mm). Gases (CH_4, O_2, and Ar) enter the grid under the inlet conditions of plug flow and travel 5 cm (upstream region) to the front heat shield under developing laminar flow. The ceramic foam sections (front heat shield, catalyst, and back heat shield, all 19 mm diameter by 10 mm long) were modeled using a homogeneous porous media approximation, which assumes local thermal equilibrium between the gas and surface [37]. Porosity was taken as 0.81 [33], and the solid component of the foam was simulated as polycrystalline alumina. Sink terms were used using the hydraulic diameter approach to account for the effect of the 80 ppi foam on the flow field by inputting isotropic inertial and viscous resistance terms for 80 ppi ceramic foams [38]. Thermal con-

ductivity in the porous zones was treated as an average between the gas and surface based on porosity.

After leaving the back heat shield, gases travelled 5 cm under developing laminar flow to the grid outlet. The boundary condition on the external surfaces of the quartz tube was adiabatic. As for the PFR model, the site density for the Rh surface was 2.72×10^{-9} mol cm^{-2} for the 38 step mechanism. Temperature-dependent transport properties in the gas phase were calculated using ideal gas kinetic theory, and the effective thermal conductivity of quartz (fused silica) and alumina from 300 to 2000 K were taken as a polynomial function of temperature [39]. Fickian diffusion was included using a dilute diffusion coefficient for each species. The effect of radiation in the calculation of the porous medium effective thermal conductivity was neglected; however, this effect should be small on 80 ppi foams compared with that of lower-cell density foams (e.g., 10–45 ppi foams) with a lower extinction coefficient [40] or packed beds with a significantly greater thermal conductivity [41]. To demonstrate this point, Sweeting et al. [42] gave an effective thermal conductivity for 45 ppi, 92% alumina foam (including the effects of conduction and radiation) of 1.28 W mK^{-1} at 1000 °C. The effective thermal conductivity in this work for a 45 or 80 ppi foam is 1.3 W mK^{-1} at 1000 °C. The neglect of the radiation effect becomes a better approximation as the ppi and extinction coefficient of the foam increase.

Converged steady-state solutions were acquired by solving the Navier–Stokes momentum, energy, and species continuity equations with a segregated, implicit solver [37] using a computational node on the IBM power 4 system at the University of Minnesota. Species coverages were computed by coupling the species continuity equations with wall surface reaction boundary conditions via a stiff, coupled solver [37]. A specific surface area of 160 cm^2 cm^{-3} was used for the porous catalyst foam without additional tuning for comparison with the PFR simulations. Specific surface areas for 80 ppi foams up to 210 cm^2 cm^{-3} have been measured with no additional washcoat [33]. Using a standard underrelaxation method, approximately 50,000 iterations and 6–10 h were required for convergence. A criterion of 10^{-6} was used for each scaled residual component (continuity, x-velocity, y-velocity, energy, species) to determine solution convergence. Solution results using convergence criteria ranging from 10^{-6} to 10^{-7} showed no significant difference in velocity, temperature, or concentrations (<1.0%), thereby validating the sufficiency of the criteria. Computational cell number in these simulations was varied to ensure that the solution was grid-independent. In addition, the second-order discretization scheme in Fluent was used to reduce the effects of numerical diffusion (discretization error) on the solution [37].

3. Results

3.1. Species and temperature profiles

According to literature results, the mechanism for methane CPO depends most strongly on the Rh oxidation state and temperature. To study the influence of these parameters, profile measurements were performed for two different flow rates (5 and 10 l min^{-1}) and three different C/O ratios (0.7, 1.0, 1.3).

3.1.1. Variation of the total flow rate

The stoichiometric C/O ratio for the methane CPO reaction (Eq. (1)) is 1.0. This ratio was chosen as basis to compare the profiles for a total flow rate of 5 and 10 l min^{-1}. Fig. 3 shows the experimental data points and the model predictions.

Both profiles look qualitatively very similar. The conversion of O_2 is very rapid and reaches completion after only 0.5 and 1.0 mm behind the catalyst entrance, for a total flow of 5 and 10 l min^{-1} respectively. Because reactions with O_2 are the only heat-providing reactions, the surface temperature should reach its maximum before or at the point of total O_2 conversion. However, the measured temperatures reach their maximum values (∼810 and ∼890 °C) significantly further downstream from this point, so that the measured T-profiles reflect gas rather than surface temperatures. This can be explained by the fact that the tip of the thermocouple is circumvented by the gas but is not in direct contact with the catalyst surface.

For both flow rates, the partial oxidation products H_2 and CO are formed partly in the oxidation zone and partly downstream from the point of total O_2 conversion in a steam-reforming zone. The H_2O traces, calculated from the O-atom balance, show H_2O formation in the oxidation zone followed by H_2O consumption in the reforming zone. The relative amounts of H_2 and CO formed in the presence of O_2 do not vary much with flow rate. For 5 and 10 l min^{-1} about 1/2 of the CO and 1/3 of the H_2 are formed in the oxidation zone, the rest in absence of O_2 by steam reforming. The profiles of H_2 and CO are nearly congruent as long as oxygen is present, resulting in an overall H_2/CO stoichiometry of 1/1. After O_2 is fully converted, the CO profiles show a pronounced drop in slope for both flows. The slopes of the H_2 profiles remain nearly uninfluenced in both cases. The H_2/CO-molar ratio approaches for both flow rates toward the end of the catalyst the partial oxidation stoichiometry of 2 (cf. Eq. (1)). CO_2 is formed in only small amounts on Rh and only as long as O_2 is present. The CO_2 concentration remains essentially constant after O_2 is fully converted. There is no significant indication of CO_2 reforming or water–gas shift. The highlighted increase of CH_4 and H_2O and the decrease of H_2 and CO for 10 l min^{-1} indicate methanation ($3H_2 + CO \rightarrow CH_4 + H_2O$) peaking at about 7.5 mm.

3.1.2. Variation of the C/O ratio

Fig. 4 compares the species and temperature profiles for a C/O ratio of 0.7 and 1.3 at a fixed total flow of 5 l min^{-1}. The profiles for 1.0 and 5 l min^{-1} are shown in Fig. 3 (left panels). As expected, the catalyst runs much hotter for C/O = 0.7 (∼1040 °C) than for 1.0 and 1.3 (both ∼810 °C). However, the O_2 conversion is four times faster at syngas stoichiometry (total conversion at 0.5 mm at C/O = 1.0) than at lower or higher C/O ratios (total conversion at 2.0 mm at C/O = 0.7 and 1.3).

A clear trend is observed in terms of catalyst length, especially by comparing the H_2 profiles for the three C/O ratios. For C/O = 0.7, the final H_2 value is reached after 5 mm. For C/O = 1.0, the H_2 plateau is reached at about 7.5 mm, whereas

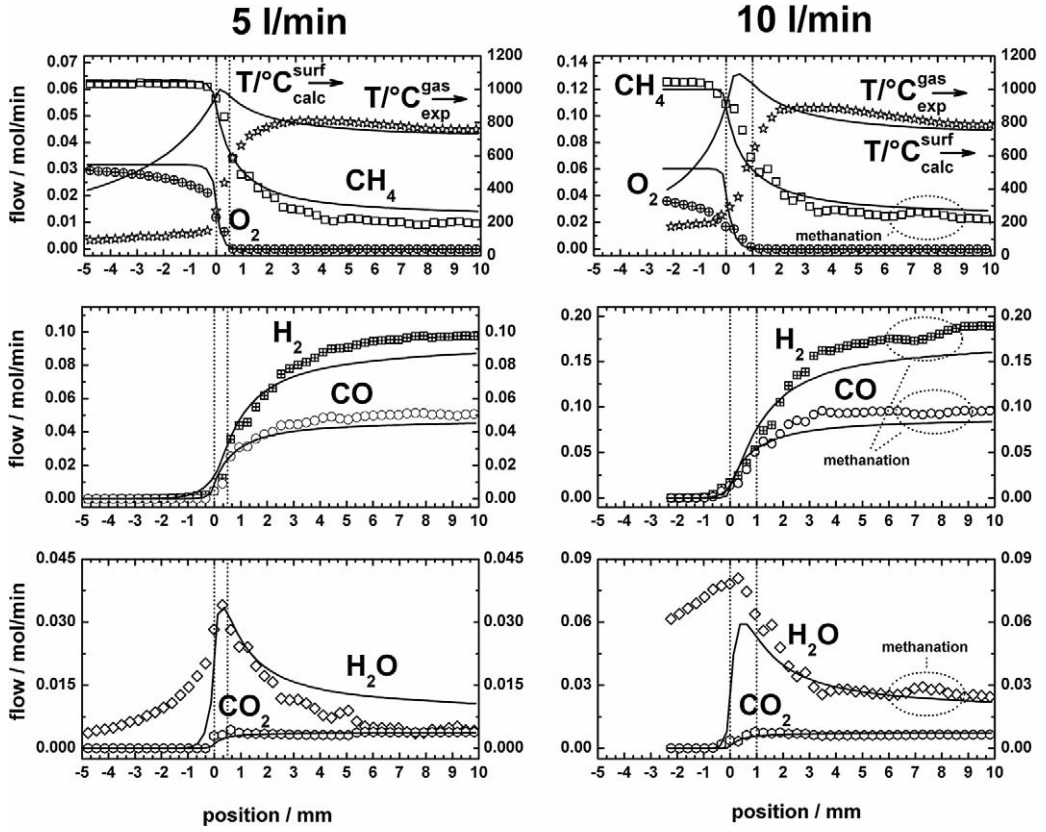

Fig. 3. Species and temperature profiles for total flow = 5 and 10 $1\,min^{-1}$, C/O = 1.0, symbols—experimental profiles ((□) CH_4, (⊕) O_2, (⊞) H_2, (○) CO, (◇) H_2O, (○) CO_2, (☆) T^{gas}), solid lines—2D porous model at centerline.

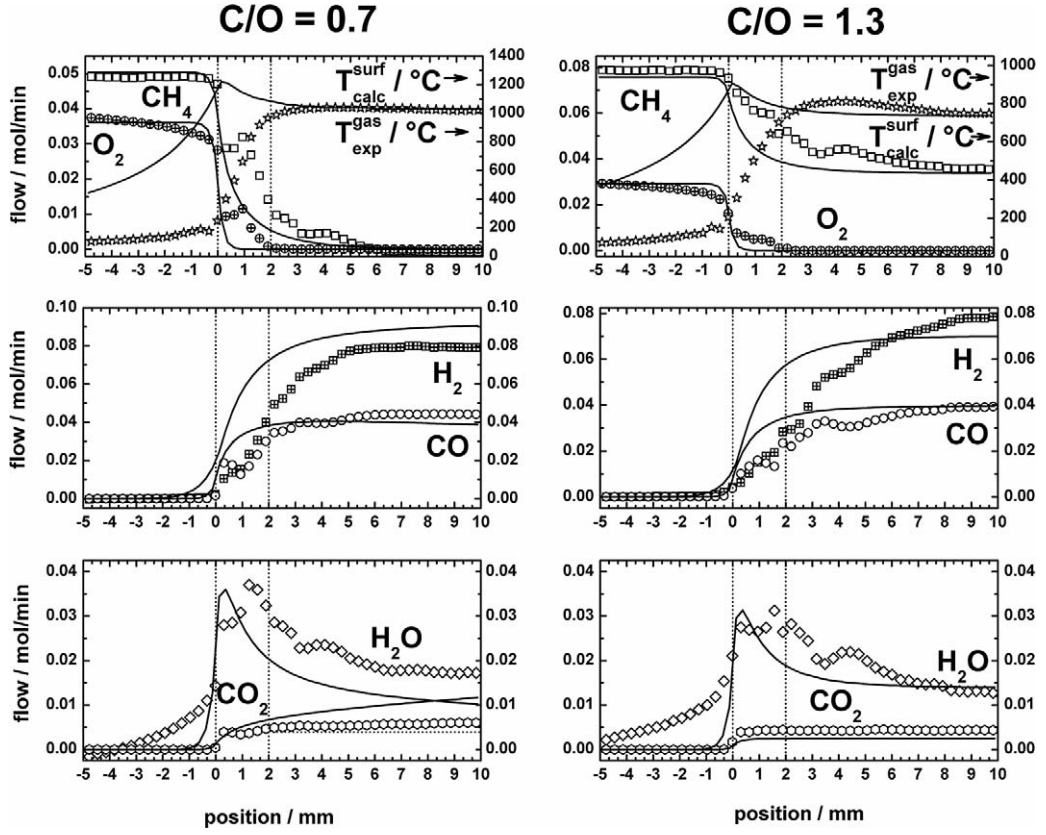

Fig. 4. Species and temperature profiles for C/O = 0.7 and 1.3, total flow = 5 $1\,min^{-1}$, symbols—experimental profiles ((□) CH_4, (⊕) O_2, (⊞) H_2, (○) CO, (◇) H_2O, (○) CO_2, (☆) T^{gas}), solid lines—2D porous model at centerline.

the full catalyst length of 10 mm is needed before H_2 levels off at $C/O = 1.3$.

In all profiles measured, the CO_2 looks like a small step. Some CO_2 is formed in the oxidation zone, but downstream the point of total O_2 consumption CO_2 is neither formed nor consumed in significant amounts. A marginal increase of CO_2 due to the water–gas shift is observed for $C/O = 0.7$ (cf. CO_2 trace with dotted horizontal line in Fig. 4 lower left panel). As already observed for $C/O = 1$ at 10 l min^{-1}, the profiles presented in Fig. 4 show an intermediate methanation at 4.0 mm for $C/O = 0.7$ and 4.5 mm at $C/O = 1.3$. The methanation will be discussed in more detail in Section 4.2.

3.2. Numerical simulations

3.2.1. Species and temperature profiles: variation of the total flow rate at $C/O = 1.0$

For a 5 l min^{-1} total flow rate, the calculated surface temperature increases from ∼400 °C at 5 mm within the front heat shield to ∼1000 °C at the catalyst entrance (Fig. 3). All of the oxygen and 40% of methane are converted within 0.5 mm (oxidation zone) where H_2O and CO_2 flow rates reach their maximum values. 30% of H_2 production and 50% of CO production are predicted in this zone. After this zone, the remaining CH_4 and H_2O combine to give significant production of more syngas through steam reforming accompanied by a decrease in the calculated temperature from 1000 °C at the end of the oxidation zone to 735 °C at the catalyst exit. The simulations show no sign of CO_2 reforming in the reforming zone under these conditions. The calculated surface temperature and experimental gas temperature equilibrate at ∼3 mm, and the calculated temperature falls below the experimental temperature for the remaining catalyst length. The major differences observed inside the catalyst are the predicted outlet CH_4 conversion and H_2O selectivity, which disagree by a few percentage points. The model correctly predicts the observed oxidation length (0.5 mm). For a 10 l min^{-1} total flow rate, the simulation correctly predicts a doubling of the oxidation length to approximately 1 mm. Doubling the total flow rate approximately doubles the magnitude of the species profiles at each axial location, as expected, and a slight increase in the peak surface temperature is predicted (1090 °C).

3.2.2. Species and temperature profiles: Variation of the C/O ratio at 5 l min^{-1} total flow

For $C/O = 0.7$, the calculated surface temperature increases from ∼450 °C at 5 mm within the front heat shield to 1220 °C at the catalyst entrance (Fig. 4). All of the oxygen and 77% of the methane are converted within 1 mm (oxidation zone), where H_2O flow rate reaches its maximum value. 62% of the H_2 and 85% CO production are predicted in this zone. After this zone, the remaining CH_4 and H_2O produce significantly more syngas through steam reforming accompanied by a decrease in the calculated temperature from 1150 °C at the end of the oxidation zone to 1030 °C at the catalyst exit. In contrast to experiments at $C/O = 1.0$, simulations show a significant water–gas shift in the reforming zone at these higher temperatures. The water–gas shift causes an increase in H_2 and CO_2 and a decrease in CO and H_2O. The calculated surface temperature and experimental gas temperature equilibrate after ∼4 mm. Fair qualitative agreement between the simulated and experimental profiles is observed. Quantitative deviation between the experimental flow rates and model is more pronounced here than at $C/O = 1.0$. The simulations predict a shorter oxidation zone than experiments (1 mm vs. 2 mm) and a faster rate of syngas production.

For $C/O = 1.3$, all of the oxygen and 40% of methane are converted within 1 mm (oxidation zone), where H_2O flow rate reaches its maximum value. 60% of the H_2 production and 73% of the CO production are predicted in this zone. After this zone, the remaining CH_4 and H_2O are shown to give significant production of more syngas through steam reforming accompanied by a decrease in the calculated temperature from 830 °C at the end of the oxidation zone to 740 °C at the catalyst exit. The calculated surface temperature and experimental gas temperature equilibrate after 3 mm, and the calculated temperature falls below the experimental temperature for the remaining catalyst length. Good qualitative agreement between the simulated and experimental profiles is observed. However, as with $C/O = 0.7$, the simulations predict a shorter oxidation zone than experiments (0.5 mm vs. 2 mm) and a faster rate of syngas production.

3.2.3. Predicted species coverages for 5 l min^{-1} total flow rate

Calculated major species coverages (>0.001) are shown for C/O ratios of 0.7, 1.0, and 1.3 (Fig. 5). For $C/O = 0.7$ characterized by calculated surface temperatures always above 1000 °C, Rh predominately covers the surface with coverage

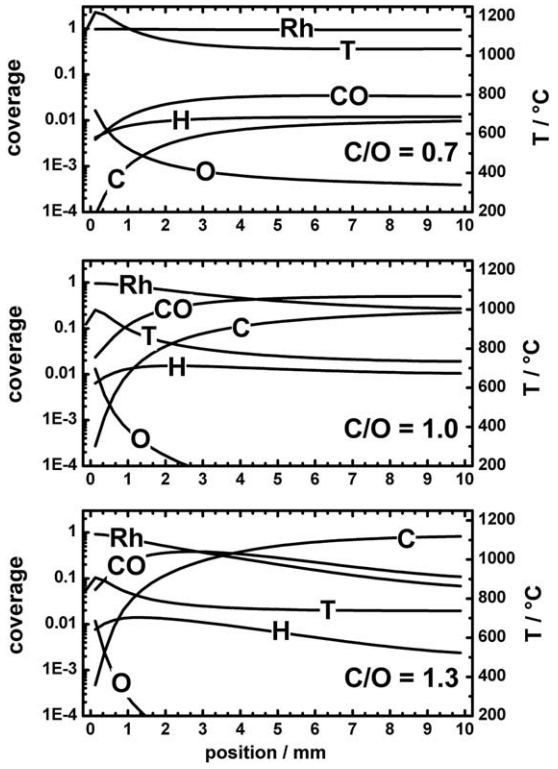

Fig. 5. 2D porous model: calculated centerline surface coverages for $C/O = 0.7$, 1.0 and 1.3, total flow = 5 l min^{-1}.

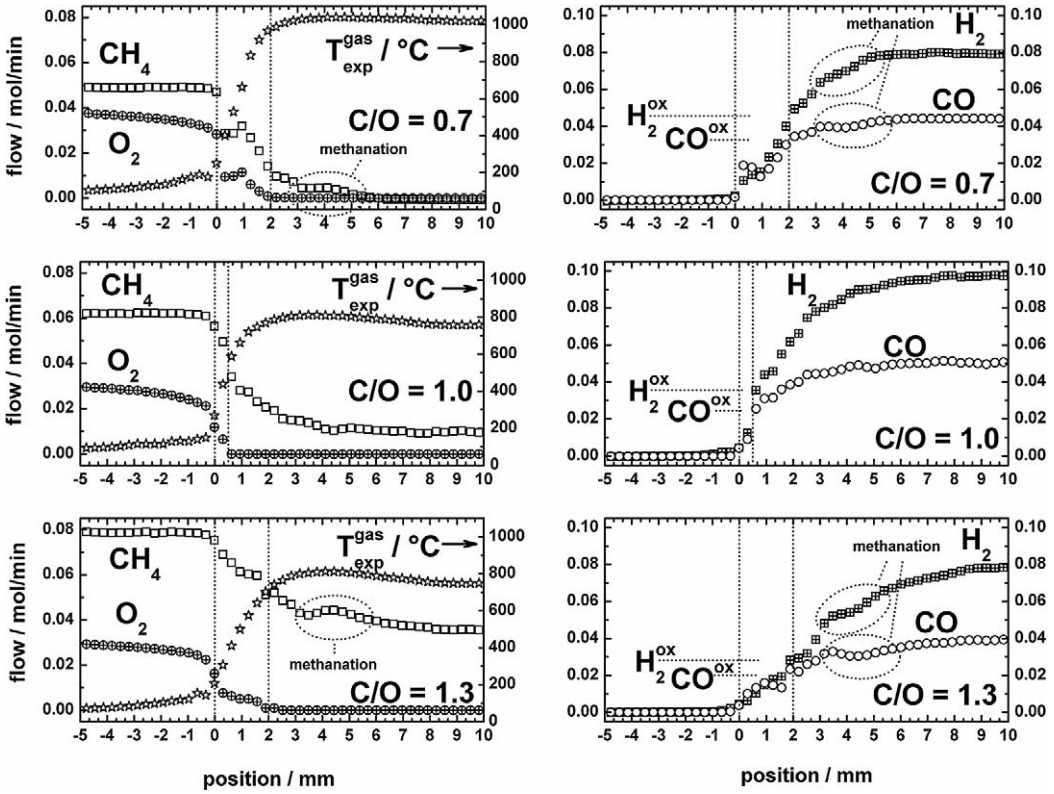

Fig. 6. Comparison of species and temperature profiles for different C/O = 0.7, 1.0 and 1.3 at total flow = 5 l min^{-1} ((□) CH_4, (⊕) O_2, (⊞) H_2, (○) CO, (☆) T^{gas}).

varying from 0.975 at the catalyst entrance to 0.95 at the outlet. Down the catalyst axis, oxygen coverage decreases from ∼0.02 to below 10^{-3} in the first 2 mm, while CO, H, and C increase in coverage from 0.004 to ∼0.035, ∼0.012 and ∼0.010 respectively at the reactor outlet. For C/O = 1.0 temperature drops to a range from 1000 °C peak to 730 °C at the reactor outlet. Species coverage hierarchy is qualitatively similar to C/O = 0.7; however, noticeable quantitative differences are observed. Rh coverage decreases significantly, varying from 0.95 at the catalyst entrance to 0.28 at the outlet. CO and C coverage increase markedly to 0.5 and 0.2, respectively, at the reactor outlet. For C/O = 1.3, the observed trend continues with temperatures ranging from ∼900 to 730 °C accompanied by a marked decrease in Rh coverage from 0.92 at the entrance to 0.07 at the outlet. CO coverage achieves a peak of 0.42 at 3 mm and then decreases, whereas C increases to 0.82 at the catalyst exit.

4. Discussion

4.1. Experimental results

Fig. 6 compares the experimental profiles for the reactants CH_4 and O_2 and the desired products H_2 and CO for all C/O ratios studied (0.7, 1.0, 1.3) and a total flow of 5 l min^{-1}. All species profiles, including those measured for C/O = 1.0 at 10 l min^{-1}, show that H_2 and CO are formed partly in the presence of oxygen and partly after total oxygen consumption by steam reforming. CO_2 reforming does not contribute to the syngas formation (cf. Figs. 3 and 4). A very small increase in CO_2 for C/O = 0.7 is observed (cf. horizontal dotted line in Fig. 4), indicating a small but nearly negligible contribution of the water–gas shift to the formation of H_2 ($CO + H_2O \rightleftarrows CO_2 + H_2$) at low C/O.

The measurements presented in this work suggest that the length of the oxidation zone depends on the total flow rate and the stoichiometry of the reactants. The fastest O_2 conversion (0.5 mm) is observed for syngas stoichiometry (C/O = 1.0, cf. Eq. (1)) and a total flow of 5 l min^{-1}. Maintaining syngas stoichiometry but doubling the flow rate to 10 l min^{-1} doubles the length of the oxidation zone. The residence time τ to reach 100% O_2 conversion remains roughly the same, but because the flow rate $\dot{V}$ is doubled, the catalyst length l required for total O_2 conversion doubles for a fixed cross-section A as well ($\tau = (l \cdot A)/\dot{V}$). Interpreting the significant longer oxidation zone at C/O = 0.7 and 1.3 (both 2 mm) is more difficult. As emphasized in Section 1.1, Rh metal sites are reportedly active for syngas formation. At low C/O ratios (e.g., 0.7) or high C/O ratios (e.g., 1.3), a considerable fraction of surface sites might be blocked by chemisorbed O_s (perhaps as Rh_xO_y [43]) or surface carbon C_s, respectively, so that it takes longer for consumption of all gas-phase O_2 than at optimal syngas stoichiometry (C/O = 1.0). Another explanation for the extended oxidation zone at C/O = 1.3 might be inhibition of the reaction by CO and H_2, which do not desorb as fast as at C/O = 1.0 because of the lower surface temperature. But all of these interpretations are purely speculative, and more experiments are necessary to establish a correlation between the length of the oxidation zone and the operation conditions. It can be concluded that the reaction is extremely rapid at C/O = 1.0 and

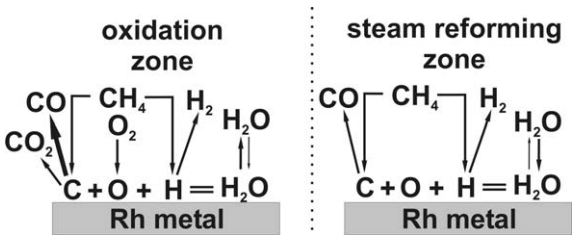

Fig. 7. Simplified two zone mechanistic picture.

that even for 10 $l\,min^{-1}$, the final gas composition is reached after about 5 mm, which for a 10 mm long catalyst leaves about half of the noble metal unused.

The amount of H_2 formed in the oxidation zone seems to depend most sensitively on temperature. For the hot catalyst at $C/O = 0.7$, about 60% of the H_2 is formed in the oxidation zone. In comparison, for all other conditions ($C/O = 1.0$ at 5 and 10 $l\,min^{-1}$, $C/O = 1.3$ at 5 $l\,min^{-1}$) with similar lower maximum temperatures between 800 and 900 °C, only 1/3 of the H_2 is formed in the presence of O_2. The same trend holds for CO. For $C/O = 0.7$, about 75% of the CO is formed in the presence of gas-phase O_2 at all other C/O ratios only 50%. For all three C/O ratios, the H_2/CO ratio at the end of the catalyst is about 2.

For all species profiles measured, the CO production rate decreases significantly at the point of 100% O_2 conversion whereas the H_2 production rate does not noticeably sense when the transition from the oxidation zone to the steam-reforming zone occurs. A simplified two-zone mechanistic picture that supports all of the experimental findings is shown in Fig. 7. Methane and oxygen adsorb dissociatively on Rh metal sites, forming C, O, and H atoms; however, the fact that the H_2 production rate is not influenced by the transition from the oxidation to the steam-reforming zone points to a quasi- equilibrium between $2H_s + O_s = H_2O_s$. Only after many cycles of H_2O formation and dissociation do two H atoms recombine and leave the surface as H_2. On the other side of the equilibrium, some water desorbs, leading to a net formation of H_2O in the oxidation zone. The situation for the CO formation is different. Surface C atoms can combine with surface O atoms both from the $2H_s + O_s = H_2O_s$ equilibrium fed by readsorption of water and from dissociative O_2 adsorption. If gas-phase oxygen is totally consumed, then O_s is replenished only by readsorption and dissociation of H_2O, and the CO production rate drops significantly. If a CO molecule stays long enough at the surface to react with another O_s, then CO_2 is formed. If the H atoms do not leave the surface quickly enough as H_2, they may do so as H_2O. At high reaction temperatures (e.g., $C/O = 0.7$), CO and H_2 can desorb more quickly, and more partial oxidation products are formed in the presence of gas phase O_2 than at low temperatures.

4.2. Fine structure and experimental artifacts

Nearly all of the species profiles measured with the newly developed capillary technique (many more than shown here) show a fine structure that is highly reproducible. Close inspection of the profiles for $C/O = 1.0$ and 10 $l\,min^{-1}$ flow rate shows methanation at ∼7.5 mm (cf. Fig. 3), and the profiles for $C/O = 0.7$ and $C/O = 1.3$ (both 5 $l\,min^{-1}$ flow rate) show methanation at 4 and 4.5 mm, respectively (cf. Fig. 6). Here H_2 and CO are consumed, and CH_4 and H_2O are formed ($3H_2 + CO \rightarrow CH_4 + H_2O$). The reason for this intermediate methanation remains unclear; it seems to be enhanced by applying a washcoat to the catalyst (not shown). Another reproducible feature is a small plateau of all species in the oxidation zone (cf. Fig. 6, $C/O = 0.7$ and 1.3). Experiments and simulations are currently under way to explore the fine structure in the profiles.

All profiles presented in this work show a more or less pronounced conversion of reactants before the start of catalysis. A positioning error of the capillary tip could falsely indicate a precatalytic conversion, but none of the profiles shows delayed conversion, making this explanation implausible, because all measurements were done on independent catalyst/capillary assemblies. More realistic is a blurring of the reaction zone onset due to diffusion of reactants into the catalyst and diffusion of products into the front heat shield. In addition, the continuous gas withdrawal by the capillary could blur the onset of the catalytic section. The precatalytic CH_4 conversion is generally weak (see Figs. 3 and 4). The precatalytic O_2 conversion is much more pronounced than CH_4, and experiments are underway to explore this difference. A possible explanation is that due to the high H_2 concentration gradient at the catalyst entrance coupled with its extraordinary high diffusivity at high temperatures, H_2 diffuses back into the channel left behind by pulling the capillary out and reacts either on the front heat shield or homogeneously with O_2 to H_2O. The porous model predicts a pronounced back-diffusion of H_2 supporting this theory (cf. Figs. 3 and 4), but it does not include precatalytic chemistry; hence H_2, not H_2O, is observed before the catalyst. The superficial flow velocity in the channel might be lowered, because shielding by the capillary amplifies the back-diffusion of H_2 even more than the model predicts. Profiles obtained with a capillary having a hole in the side leaving the channel filled at all points show a significantly reduced precatalytic O_2 conversion comparable to that of CH_4.

4.3. Agreement with numerical simulations

All simulated profiles shown in Figs. 3 and 4 were calculated with the 2D porous model to include the effects of axial heat conduction in the quartz tube and the alumina support. Neglecting the effect of wall heat conduction seriously affects the predicted reactor yields [44].

A fair qualitative agreement between simulated and measured species profiles is observed for all experimental conditions. The formation of H_2 and CO, both in the presence of gas-phase O_2 and after total O_2 conversion by steam reforming, is predicted correctly. Good quantitative agreement is obtained for $C/O = 1.0$; some quantitative deviations are observed for $C/O = 0.7$ and 1.3. Especially at $C/O = 0.7$ the model predicts more water–gas shift ($CO + H_2O \rightarrow CO_2 + H_2$) than was experimentally observed.

For all experimental conditions, calculated and experimental temperatures are largely different until they equilibrate a few mm behind the catalyst entrance. The differences can be explained when comparing these simulations in light of previous work solving energy equations for both the gas and solid phases for fixed bed [29]. In the present simulations, only one energy equation is solved for both surface and gas (local thermal equilibrium), because surface temperature dictates the chemistry. Based on the work in [29], large temperature gradients between gas and surface exist in the catalyst entrance region. The calculated temperatures in this work are in good agreement with surface temperatures predicted and measured in [29]. The experimental temperatures measured in the present work are largely skewed toward the gas phase. In agreement with the slight differences between the measured (gas) and calculated (surface) temperatures in the reforming zone, it has been previously shown that in the reforming section of the catalyst, the gas temperature should be slightly higher than the surface temperature because of endothermic chemistry occurring at the surface and interphase heat transport [29].

At all experimental conditions, the model predicts a decrease in the reactant molar flow rates and an increase in the product molar flow rates before the catalyst entrance, in qualitative agreement with the experiments. Axial diffusion caused by the high temperatures and large concentration gradients in the entrance region cannot be ignored if precatalytic reactant conversion is to be resolved.

Quantitative species agreement between experiments and simulations become worse at $C/O = 0.7$ and 1.3. Oxidation zone length (1 mm) predicted at both C/O ratios is shorter than those found in the experiments (2 mm). The rates of syngas production and CH_4 and H_2O consumption is much faster in the simulations that shown by the experiments. However, these observations may be explained by very different reasons for the two feed ratios. At $C/O = 0.7$, because the mechanism does not consider rhodium oxide, the mechanism may predict more rapid methane activation than actually occurs in experiments, due to the increased oxygen composition in the gas phase when operating at this C/O. At $C/O = 1.3$, carbon coverage may be more pronounced at the catalyst entrance than that predicted by the model giving lower initial catalyst activity and a more gradual reaction rate than shown by the simulations. Because of the greater extent of water–gas shift occurring in the simulation than was observed experimentally at $C/O = 0.7$, deviation between the product flow rates for the experiments and model is more pronounced than at $C/O = 1.0$. Because $C/O = 1.0$ is the canonical composition for this mechanism's refinement, further refinement is needed to account for these effects.

4.4. Reactor model and mechanism refinement

To simulate the profiles in the reactor sufficiently, both the right reaction mechanism and an appropriate reactor model are important. Fig. 8 compares adiabatic 2D and PFR simulations. An inlet temperature (500 °C) giving the same oxidation length observed in the experiments for $C/O = 1.0$ and 5 l min^{-1} flow rate was chosen for the PFR model. The comparison shows that considering heat conduction in the reactor wall and catalyst has a dramatic effect on the temperature and hence on the species profiles. In addition, axial diffusion must be included in the model to accurately predict the inlet section of the catalyst.

The adiabatic PFR model predicts a dramatically higher peak temperature than the 2D model and thus shows much faster development of the species profiles to their final steady-state values. Because the experimental temperature profiles in this work reflect the gas-phase temperature, which is lower than the surface temperature, using them as input into a PFR model leads to an overprediction of the oxidation section length (1.5 mm vs. 0.5 mm) and a delayed development of the species profiles (data not shown).

The authors of the recently published 104 reaction step mechanism [32] used experimental temperature profiles from

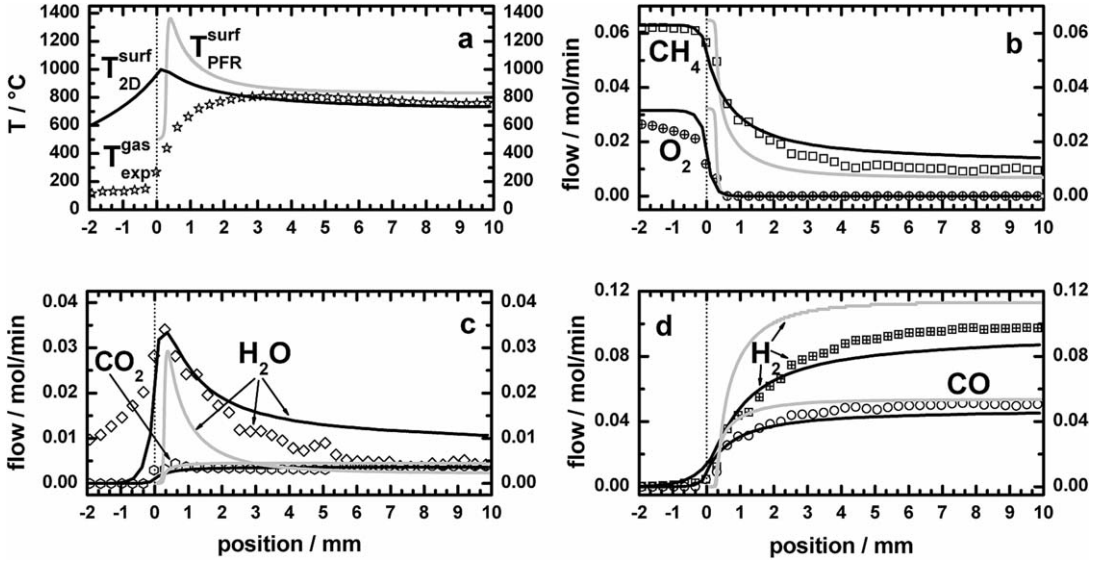

Fig. 8. Comparison of the PFR (gray solid line) and the 2D porous reactor model (black solid line): (a) temperature profiles (experimental T^{gas} (☆)), (b)–(d) species profiles (experimental (□) CH_4, (⊕) O_2, (⊞) H_2, (○) CO, (◇) H_2O, (○) CO_2), $C/O = 1.0$, total flow = 5 l min^{-1}.

[6] as input in their PFR model for mechanism validation. The temperature values measured in [6] are similar to those found in the present work and most likely represent the gas-phase temperature, not the surface temperature. Based on the assignment of this temperature profile to the surface, it was concluded from the simulations that H_2 was produced strictly in the reforming zone, whereas CO was produced in both oxidation and reforming zones. This conclusion is in disagreement with our results and also in disagreement with the data presented in [6], which show some H_2 formation in the oxidation zone. Adiabatic PFR simulations with the 104 step mechanism show that this mechanism also predicts H_2 formation in the oxidation zone when the temperature is above 1000 °C (data not shown).

5. Conclusions

The species and temperature profiles presented in this work are the first profiles published for methane CPO on Rh-coated foams. A spatial resolution of (0.3 mm) was reached. The profiles clearly show that under technically relevant conditions (autothermal operation, up to 10 l min^{-1} flow), syngas is formed by a combination of direct partial oxidation and steam reforming. Numerical simulations using the 38 surface reaction mechanism with a 2D porous reactor model including heat and mass transfer reproduce the experimental species and temperature profiles well. Good qualitative agreement is obtained for all experimental conditions, and quantitative agreement is good for syngas stoichiometry. The model deviates somewhat for lower ($C/O = 0.7$) and higher ($C/O = 1.3$) C/O ratios. The current work reinforces the need to compare numerical simulations to sufficiently resolve experimental profiles to verify the validity of the reaction mechanism and the reactor model, and motivates further work on mechanism refinement.

Acknowledgments

R.H. acknowledges funding through an Alexander von Humboldt Foundation Feodor Lynen Fellowship. The authors acknowledge financial support by the Department of Energy. K.A.W. thanks the Minnesota Supercomputer Institute for the generous computational resources and partial support of this work and A.B. Mhadeshwar and D.G. Vlachos for sharing their C1 mechanism on Rh.

References

[1] T.S. Ahlbrandt, Int. Geol. Rev. 44 (2002) 1092–1104.
[2] D.J. Wilhelm, D.R. Simbeck, A.D. Karp, R.L. Dickenson, Fuel Process. Technol. 71 (2001) 139–148.
[3] S. Freni, G. Calogero, S. Cavallaro, J. Power Sources 87 (2000) 28–38.
[4] D.A. Hickman, L.D. Schmidt, Science 259 (1993) 343–346.
[5] A.P.E. Yorck, T. Xiao, M.L.H. Green, Top. Catal. 22 (2003) 345–358.
[6] M. Lyubovsky, S. Roychoudhury, R. LaPierre, Catal. Lett. 99 (2005) 113–117.
[7] E.P.J. Mallens, J.H.B.J. Hoebink, G.B. Marin, J. Catal. 167 (1997) 43–56.
[8] H. Heitnes Hofstad, J.H.B.J. Hoebink, A. Holmen, G.B. Marin, Catal. Today 40 (1998) 157–170.
[9] W.Z. Weng, M.S. Chen, Q.G. Yan, et al., Catal. Today 63 (2000) 317–326.
[10] L. Basini, K. Aasberg-Petersen, A. Guarinoni, M. Østberg, Catal. Today 64 (2001) 9–20.
[11] C.T. Au, H.Y. Wang, J. Catal. 167 (1997) 337–345.
[12] W.Z. Weng, Q.G. Yan, C.R. Luo, et al., Catal. Lett. 74 (2001) 37–43.
[13] J.C. Slaa, R.J. Berger, G.B. Marin, Catal. Lett. 43 (1997) 63–70.
[14] D. Wang, O. Dewaele, A.M. De Groote, G.F. Froment, J. Catal. 159 (1996) 418–426.
[15] K. Nakagawa, N. Ikenaga, T. Kobayashi, T. Suzuki, J. Catal. 186 (1999) 405–413.
[16] O.V. Buyevskaya, D. Wolf, M. Baerns, Catal. Lett. 29 (1994) 249–260.
[17] H.Y. Wang, E. Ruckenstein, J. Phys. Chem. B 103 (1999) 11327–11331.
[18] Z. Tian, O. Dewaele, G.B. Marin, Catal. Lett. 57 (1999) 9–17.
[19] S. Rabe, T.-B. Truong, F. Vogel, Appl. Catal. A Gen. 292 (2005) 177–188.
[20] E. Ruckenstein, H.Y. Wang, J. Catal. 187 (1999) 151–159.
[21] D.A. Hickman, L.D. Schmidt, AIChE J. 39 (1993) 1164–1177.
[22] O. Deutschmann, L.D. Schmidt, AIChE J. 44 (1998) 2465–2477.
[23] C.T. Goralski, R.P. O'Connor, L.D. Schmidt, Chem. Eng. Sci. 55 (2000) 1357–1370.
[24] G. Veser, J. Fraunhammer, Chem. Eng. Sci. 55 (2000) 2271–2286.
[25] S. Tummala, Ph.D. Thesis, University of Minnesota (2000).
[26] E.J. Klein, S. Tummala, L.D. Schmidt, Stud. Surf. Sci. Catal. 136 (2001) 245–250.
[27] J. Wei, E. Iglesia, J. Catal. 225 (2004) 116–127.
[28] O. Deutschmann, R. Schwiedernoch, L.I. Maier, D. Chatterjee, Stud. Surf. Sci. Catal. 136 (2001) 251–258.
[29] M. Bizzi, G. Saracco, R. Schwiedernoch, O. Deutschmann, AIChE J. 50 (2004) 1289–1299.
[30] R. Schwiedernoch, S. Tischer, C. Correa, O. Deutschmann, Chem. Eng. Sci. 58 (2003) 633–642.
[31] K.A. Williams, C.A. Leclerc, L.D. Schmidt, AIChE J. 51 (2005) 247–260.
[32] A.B. Mhadeshwar, D.G. Vlachos, J. Phys. Chem. B 109 (2005) 16819–16835.
[33] M.V. Twigg, J.T. Richardson, Chem. Eng. Res. Des. 80 (2002) 183–189.
[34] R.J. Kee, F.M. Rupley, J.A. Miller, Chemkin III: A Fortran Package for the Analysis of Gas-Phase Chemical and Plasma Kinetics, 1999.
[35] R.J. Kee, F.M. Rupley, J.A. Miller, et al., Plug: A Program for the Analysis of Plug-Flow Reactors with Gas-Phase and Surface Chemistry, CHEMKIN Collection, 3.5, Reaction Design, San Diego, CA, 1999.
[36] O. Deutschmann, C.C.S. Tischer, D. Chatterjee, S. Kleditzsch, V.M. Janardhanan, DETCHEM software package, second ed., Karlsruhe, 2005, http://www.detchem.com.
[37] Fluent 6.2, Computational Fluid Dynamics Software, User's Guide, 2005.
[38] J.T. Richardson, Y. Peng, D. Remue, Appl. Catal. A Gen. 204 (2000) 19–32.
[39] F.P. Incropera, D.P. DeWitt, Fundamentals of Heat and Mass Transfer, Wiley, New York, 1996.
[40] C.Y. Zhao, T.J. Lu, H.P. Hodson, J.D. Jackson, Mater. Sci. Eng. A Sruct. A 367 (2004) 123–131.
[41] K.L. Hohn, L.D. Schmidt, Appl. Catal. A Gen. 211 (2001) 53–68.
[42] T.B. Sweeting, D.A. Norris, L.A. Strom, J.R. Morris, Mater. Res. Soc. Symp. Proc. 368 (1995) 309–314.
[43] J.-D. Grunwaldt, A. Baiker, Catal. Lett. 99 (2005) 5–12.
[44] M.J. Stutz, D. Poulikakos, Chem. Eng. Sci. 60 (2005) 6983–6997.